JOURNAL OF GEOPHYSICAL RESEARCH, VOL. 103, NO. D6, PAGES 6427–6437, MARCH 27, 1998

Observational limits for lidar, radar, and airglow imager measurements of gravity wave parameters

Chester S. Gardner
Department of Electrical and Computer Engineering, University of Illinois at Urbana-Champaign

Michael J. Taylor
Space Dynamics Laboratory, Utah State University, Logan

Abstract. By examining the observational limits and biases for lidar, radar, and airglow imager measurements of middle atmosphere gravity waves, we provide plausible explanations for the characteristics of the monochromatic wave parameters that have been reported during the past decade. The systematic dependencies of vertical and horizontal wavelength on wave period, reported in many lidar and some radar studies, are associated with diffusive damping. The prominent waves with the largest amplitudes, most often observed by lidars and radars, are those with vertical phase speeds near the diffusive damping limit. The narrow range of horizontal phase velocities of the waves seen by OH imagers is a consequence of the combined effects of the gravity wave spectrum and the OH layer response to wave perturbations. The strongest airglow fluctuations are associated with waves having vertical wavelengths comparable to the width of the OH layer. These waves have fast horizontal phase speeds near 70 m/s. Simple formulas which describe the regions of the wave spectrum observed by each instrument are derived and compared with published data. Lidars, radars, and imagers are often most sensitive to waves in largely different regions of the spectrum so that their measurements are truly complementary. However, these ground-based techniques are often incapable of observing the large-scale waves with periods longer than about 5 hours and both long vertical (>15 km) and horizontal (>1000 km) wavelengths. Spaceborne instruments, such as the high-resolution Doppler imager (HRDI) and wind imaging interferometer (WINDII) on UARS, are the techniques most likely to provide the key observations of the low wavenumber, low-frequency region of the gravity wave spectrum.

1. Introduction

Lidars, radars, and airglow imagers are used widely to study gravity waves in the middle atmosphere. For more than 3 decades, radars have provided a wealth of data on individual wave characteristics and on the spectra of quasi-random wave perturbations. Rayleigh and Na lidars have complemented these observations by providing similar data on the smaller-scale waves throughout the stratosphere and mesosphere. More recently, modern airglow imagers equipped with sensitive low-noise CCD arrays have provided crucial data on the horizontal structure and propagation directions of mesospheric gravity waves. *Reid* [1986] and *Manson* [1990] summarized the characteristics of numerous quasi-monochromatic waves measured in the mesopause region by a variety of radars, lidars, and imagers. Most of those measurements were obtained using extended time sequences at single heights (imagers) and multiple-station or beam swinging (radars) cross-spectral methods. Their data exhibited modest clustering at certain wavelengths and periods that is believed to represent unique biases and limitations associated with each measurement technique. Rayleigh and Na lidar observations display remarkably systematic relationships between the wave periods, wavelengths, and amplitudes [e.g., *Gardner and Voelz*, 1987; *Beatty et al.*, 1992; *Collins et al.*, 1996]. Similar relationships between monochromatic wave parameters are now emerging from the large body of observations obtained during the past 5 years with modern airglow imagers [e.g., *Hecht et al.*, 1993, 1994; *Swenson et al.*, 1995; *Taylor et al.*, 1991a, b, 1995a, b].

In this paper we examine the measurement limits and biases of some of these instruments and provide plausible explanations for the characteristics of the wave parameters that have been reported. We show that the systematic dependencies of the vertical and horizontal wavelengths on wave period seen in the lidar and some radar data are related to diffusive damping of the waves. We also show that the narrow range of fast horizontal phase velocities of

Copyright 1998 by the American Geophysical Union.

Paper number 97JD03378.
0148-0227/98/97JD-03378$09.00

waves seen by OH imagers is associated with the combined effects of the gravity wave spectrum and the OH layer response to wave perturbations. We derive simple formulas to describe the regions of the wave spectrum observed by each instrument and compare the predictions with observational data. These results illustrate that lidars, radars, and imagers are often most sensitive to waves in largely different regions of the spectrum so that their measurements are truly complementary.

2. OH Airglow Response to Gravity Wave Perturbations

The Meinel Band vibrational spectrum of excited OH arises from the reaction

$$H + O_3 \Rightarrow OH^* + O_2. \quad (1)$$

During the past decade, numerous groups have developed and tested sophisticated numerical models of the OH airglow response to gravity wave perturbations [e.g., *Hickey*, 1988a, b; *Lopez-Moreno et al.*, 1987; *Makhlouf et al.*, 1995; *Schubert and Walterscheid*, 1988; *Schubert et al.*, 1991; *Tarasick and Shepherd*, 1992; *Walterscheid et al.*, 1987]. Most studies are based on the work of *Good* [1976] and *McDade et al.* [1987] who made extensive comparisons of rocket measurements with various models of the mesospheric hydrogen/ozone reaction. The numerical models have shown that the intensity perturbations observed by a ground-based imager depend primarily on the amplitude and vertical wavelength of the wave. Airglow instruments are most sensitive to waves with vertical wavelengths comparable to or larger than the layer widths. In this issue, *Swenson and Gardner* [this issue] characterize the OH layer response to monochromatic gravity waves by employing the *McDade et al.* [1987] "sudden death" quenching scheme which is applicable to the high v OH^* Meinel Band emissions. By modeling the atomic oxygen profile as a Chapman layer and neglecting the wave-induced redistribution of ozone, they derived relatively simple analytic expressions for the observed emission intensity and rotational temperature perturbations as functions of the wave and OH layer parameters. Their predictions of the OH wave amplitudes and Krassovsky's ratio compare favorably to reported measurements and to values predicted by the various numerical models.

By using *Swenson and Gardner*'s [this issue] equations (46) and (49), we find that the mean square OH intensity perturbation measured by a ground-based zenith-pointing imager or photometer is given approximately by

$$\frac{<\Delta I(m,\omega)^2>}{<I>^2} \approx 7.3\exp(-m^2\sigma_{OH}^2)\frac{<\rho'(m,\omega)^2>}{<\rho>^2} \quad (2)$$

where $m = 2\pi/\lambda_z$ is the vertical wavenumber, λ_z is the vertical wavelength, ω is the frequency, $\sigma_{OH} \approx 4.4$ km is the nominal rms thickness of the unperturbed OH^* layer, and $<\rho'(m,\omega)^2>/<\rho>^2$ is the mean square relative density amplitude of the wave. Equation (2) is a simplified version of the more exact expression given by Swenson and Gardner, but it is sufficient for our purposes. Notice that the mean square OH^* response is almost an order of magnitude larger than the atmospheric density response for waves with large vertical wavelengths. However, because of the exponential term in (2), the response is significantly attenuated for $m \geq 1/\sigma_{OH}$. The attenuation results because the positive and negative volume emission rate fluctuations of the shorter wavelengths cancel each other when integrated throughout the whole OH^* layer. As a result, zenith-pointing OH imagers, photometers, and spectrometers are only sensitive to waves with long vertical wavelengths.

The $\exp(-m^2\sigma^2_{OH})$ form for the cutoff in (2) was derived analytically by *Swenson and Gardner* [this issue]. Extensive comparisons with observations were shown to be consistent with this model. Numerical models can also be used characterize the response of the OH intensity perturbations as a function of vertical wavenumber. For example the numerical computations of *Schubert et al.* [1991] also show that the response is attenuated significantly when the vertical wavelength becomes smaller than the OH layer thickness. However, their results suggest that the form for the cutoff may be more accurately approximated by $\exp(-m\,\sigma_{OH})$. Regardless of the form of this cutoff response, the results of our analysis will not be affected qualitatively. The important issue is that OH intensity response is severely attenuated for vertical wavelengths significantly smaller than the layer thickness. Some quantitative predictions can be influenced by the form of the cutoff, but these are not the focus of our analysis.

The mean square wave amplitude is related to the relative density spectrum.

$$\frac{<\rho'(m,\omega)^2>}{<\rho>^2} = F_\rho(m,\omega)\Delta m\Delta\omega/(2\pi)^2 \quad (3)$$

Δm is the vertical wavenumber bandwidth, and $\Delta\omega$ is related to Δm through the gravity wave dispersion relations

$$\Delta\omega = \frac{\omega}{m}\Delta m. \quad (4)$$

By combining (2)-(4) we have

$$\frac{<\rho'(m,\omega)^2>}{<\rho>^2} = \frac{\omega}{m}F_\rho(m,\omega)\Delta m^2/(2\pi)^2 \quad (5)$$

and

$$\frac{<\Delta I(m,\omega)^2>}{<I>^2} \approx 7.3\exp(-m^2\sigma_{OH}^2)\frac{\omega}{m}F_\rho(m,\omega)\Delta m^2/(2\pi)^2. \quad (6)$$

3. Lidar and Radar Measurements

In contrast to the airglow instruments, lidars and radars are sensitive to all waves whose observed periods and vertical wavelengths are compatible with the resolution limits and observing ranges of the instruments. Rayleigh

and Na lidars measure the relative atmospheric density, temperature, or horizontal wind profiles depending on the lidar configuration, while radars typically measure the wind profiles. The observed mean square wave amplitudes for monochromatic waves are given by (5) or by

$$< T'(m,\omega)^2 > = \frac{\omega}{m} F_T(m,\omega)\Delta m^2 /(2\pi)^2 \quad (7)$$

$$< u'(m,\omega)^2 > = \frac{\omega}{m} F_u(m,\omega)\Delta m^2 /(2\pi)^2 \quad (8)$$

where F_T and F_u are the temperature and horizontal wind spectra, respectively.

4. Gravity Wave Spectra Models

Existing theories of gravity wave spectra invoke a variety of different physical mechanisms for dissipating wave energy including shear and convective instabilities, cascade processes, wave-induced Doppler effects, and wave-induced diffusion. A detailed discussion of the leading wave dissipation paradigms and their predictions is given by *Gardner* [1996]. All of these models predict the same form and behavior for the vertical wavenumber spectrum of horizontal winds. The canonical spectrum is characterized by a vertical wavenumber m_* that partitions the spectrum into a low wavenumber regime dominated by the gravity wave source characteristics, and a high wavenumber region dominated by saturation and dissipation processes. In the source region ($m < m_*$) the spectrum is usually assumed to be proportional to m^s, where $s \approx 3/2$. In the so-called saturation region ($m > m_*$), the spectrum is proportional to N^2/m^3. Because m_* is proportional to $N/u'_{\rm rms}$, where N is the buoyancy frequency and $u'_{\rm rms}$ is the rms total horizontal wind perturbation, m_* decreases with increasing altitude as $u'_{\rm rms}$ increases. For the mesopause region the characteristic vertical wavenumber $\lambda_z^* = 2\pi/m_*$ varies between about 10 and 16 km depending on the wave activity. The leading models all assume that the temporal frequency spectrum is proportional ω^{-p}, where $p = 5/3$ or 2.

Only the Linear Instability Theory (LIT) paradigm, originally described by *Dewan and Good* [1986], and the Diffusive Filtering Theory (DFT) paradigm, formulated by *Gardner* [1994, 1995], have been developed in sufficient detail to characterize all the joint spectra, including the (m, ω) spectra, which we require in (6)-(8). In its current form the LIT model for the (m, ω) spectrum of horizontal winds, temperature, or relative atmospheric density is separable. For density the joint spectrum is given by

$$F_\rho(m,\omega) = (2\pi)^2 \frac{<(\rho')^2>}{<\rho>^2} \frac{2(s+1)}{(s+3)m_*}\left(\frac{m}{m_*}\right)^s \frac{(p-1)}{f}\left(\frac{f}{\omega}\right)^p \qquad m < m_*$$

$$(2\pi)^2 \frac{<(\rho')^2>}{<\rho>^2} \frac{2(s+1)}{(s+3)m_*}\left(\frac{m_*}{m}\right)^3 \frac{(p-1)}{f}\left(\frac{f}{\omega}\right)^p \qquad m > m_* \quad (9)$$

where

$$m_*^2 \approx N^2 / <(u')^2> \quad (10)$$

f is the inertial frequency, and $<(u')^2>$ and $<(\rho')^2>/<\rho>^2$ are the total horizontal wind and relative atmospheric density variances, respectively, of the gravity wave field.

Separability is a direct mathematical consequence of the physical mechanisms that are assumed to control energy dissipation in Linear Instability Theory. *Dewan and Good* [1986] assumed that the saturation wind amplitude of each wave packet is approximately equal to the intrinsic horizontal phase speed N/m, regardless of the frequency or horizontal wavenumber. This leads to the familiar N^2/m^3 form for the m spectrum of horizontal winds. Because wave packets reach their saturation limits more or less independently of each other, the derivations employed by Dewan and Good can also be applied selectively to all waves of any given frequency with the same N^2/m^3 result. Thus LIT implies that the shape of the m spectrum does not depend on wave frequency, at least for $m > m_*$, although the magnitude may. In other words, the joint (m, ω) spectrum of horizontal winds is separable. This attribute is a direct consequence of the assumption that saturation is independent of frequency and horizontal wavenumber; that is, it depends only on N/m.

In the development of the DFT spectral models, waves are assumed to be severely damped when the vertical velocity of momentum diffusion (mD_{zz}) exceeds the vertical phase velocity of the wave (ω/m), where D_{zz} is the effective diffusivity of the atmosphere. DFT joint spectra are not separable because the wave damping criterion ($\omega/m = mD_{zz}$) depends on both m and ω. The consequences of the damping limit on the joint spectrum are illustrated in Figure 1a. Waves lying to the right of the diagonal line are severely damped by diffusion because of their slow vertical phase speeds. These waves are eliminated from the spectrum. The DFT joint spectra have the form [*Gardner*, 1994]

$$F_\rho(m,\omega) = (2\pi)^2 \frac{<(\rho')^2>}{<\rho>^2} \frac{(s+1)}{m_*}\left(\frac{m}{m_*}\right)^s \frac{(p-1)}{f}\left(\frac{f}{\omega}\right)^{p+(s+1)/2} \qquad m \le m_*(\omega/f)^{1/2} = (\omega/D_{zz})^{1/2} \quad (11)$$

where

$$m_*^2 = f / D_{zz}. \quad (12)$$

The DFT ω spectra of relative density, temperature, and horizontal winds are proportional to ω^{-p}, while the m spectra are proportional to $m^{-(2p-1)}$ in the region $m>m_*$. For $p = 2$, they are proportional to ω^{-2} and m^{-3}, and D_{zz} becomes

$$D_{zz} = \frac{(s+1)}{(s+3)} f \ln(N/f) \frac{<(u')^2>}{<(\partial u'/\partial z)^2>}, \quad p = 2. \quad (13)$$

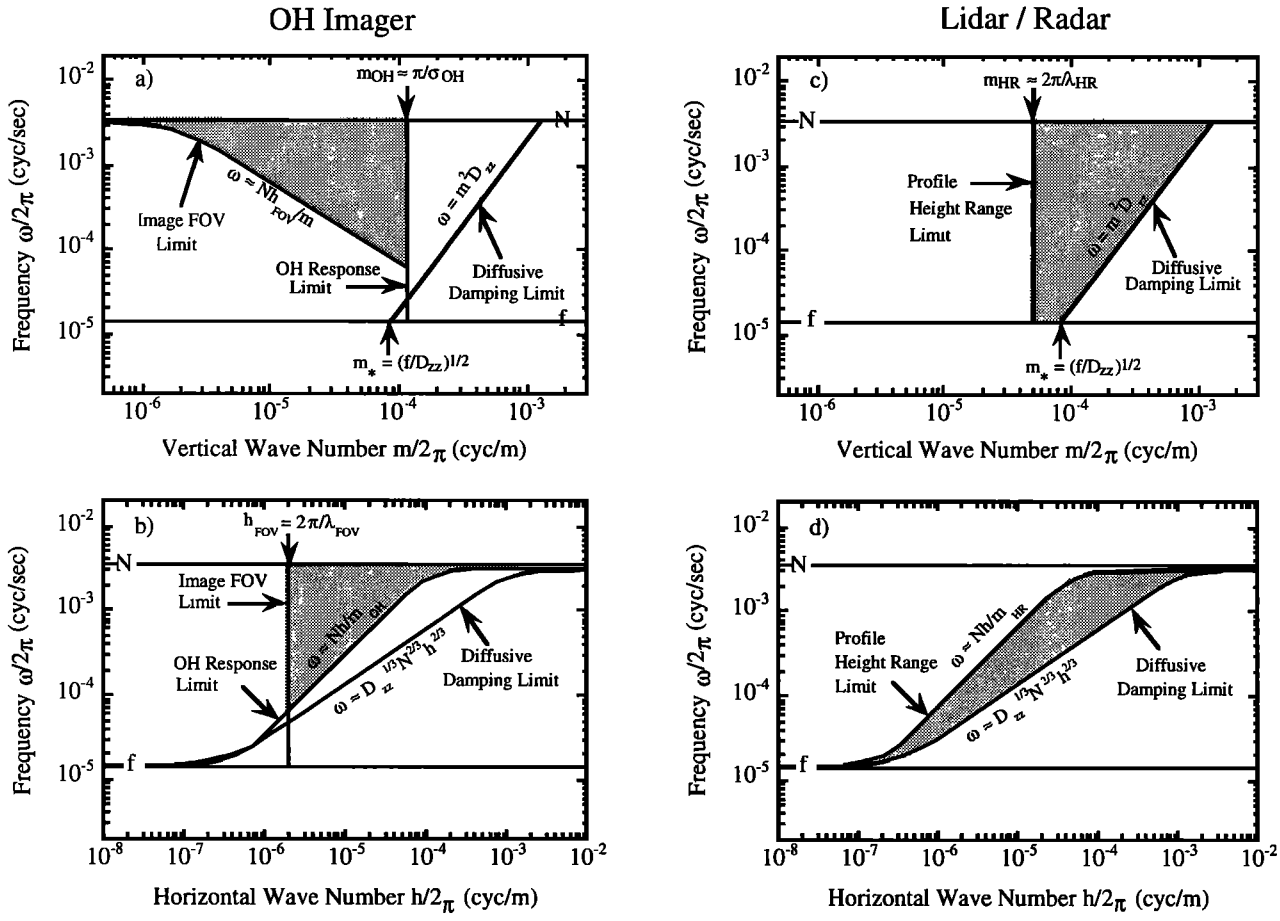

Figure 1. (a) The (ω, m) and (b) (ω, h) spectrum observation limits for OH imagers. (c) The (ω, m) and (d) (ω, h) spectrum observation limits for lidars and radars using sequences of height profiles to infer gravity wave parameters. These instruments are sensitive to gravity waves lying in the shaded spectral regions. The observation limits are plotted for σ_{OH} = 4.4 km, λ_{FOV} = 500 km, λ_{HR} = 20 km, λ_z^* = 12 km, and D_{zz} = 320 m^2/s.

5. Observational Limits of OH Imagers

OH imagers use fisheye lenses to focus all-sky images onto CCD detector arrays. Typical integration times are about 60 s, and an additional 30 to 60 s are required to transfer the image to permanent storage. Images are usually acquired continuously every few minutes during the night so that the instruments are sensitive to waves with periods as short as the buoyancy period. Depending on the approach used to compute the intensity perturbations, imagers are sensitive to gravity waves with periods as long as the observation period or potentially even the inertial period. For our studies, we will assume that the imager is sensitive to all gravity waves with frequencies between f and N. The horizontal resolution varies throughout the field of view because of distortion caused by the imaging geometry and the fisheye lens. Typical values range from approximately 0.5 km at zenith to approximately 10 km at 300 km radial distance from zenith. Because of severe distortion at low-elevation angles, image analysis is usually restricted to the central 500 to 600 km field of the image. In this case, the observations include waves with horizontal wavelengths as small as about 1 km and and as large as the imager field of view (FOV) λ_{FOV}. For our study, we assume $\lambda_{FOV} \approx 500$ km. A detailed discussion of the imager resolution limitations, distortion, and data processing is given by *Coble et al.* [1997].

The mean square relative intensity amplitudes of the waves observed by zenith-pointing OH airglow instruments can be calculated by substituting the model for the density spectrum into equation (6). We consider first the DFT model spectrum.

$$\frac{<\Delta I(m,\omega)^2>}{<I>^2} \propto \exp(-m^2\sigma_{OH}^2)\left(\frac{m}{m_*}\right)^{s-1}\left(\frac{f}{\omega}\right)^{p+(s-1)/2}$$

$$m \le m_*(\omega/f)^{1/2} \qquad (14)$$

As we noted previously, imagers are only sensitive to waves with the longer vertical wavelengths because of the exponential term on the right-hand side of (14). The actual cutoff limit depends on the wave amplitude and the noise

characteristics of the imager. Modern broadband OH imagers are capable of observing waves with intensity amplitudes as small as a few tenths percent. Waves with vertical wavelengths ~10 km typically have density amplitudes of 5-10%. A simple calculation using equation (2) gives a value $\sim\pi/\sigma_{OH}$ for the OH response cutoff wavenumber m_{OH}. The OH intensity perturbations induced by waves with vertical wavenumbers larger than m_{OH} are not large enough to be detected by the imager. This cutoff is plotted in Figures 1a and 2a. Since $\sigma_{OH} \approx 4.4$ km [*Swenson and Gardner*, this issue], the OH cutoff wavelength $2\sigma_{OH}$ is only slightly smaller than the characteristic vertical wavelength λ_z^* so that m_{OH} lies very near m_*. Imagers are sensitive primarily to waves in the source region of the vertical wavenumber spectrum. We emphasize, however, that m_{OH} does depend on the imager signal-to-noise ratio (snr). Imagers with higher snr's will have higher values for m_{OH} because they are capable of resolving smaller-amplitude variations in the images.

Because imagers observe the horizontal structure of the waves directly, it is more convenient to transform (14) to the (h, ω) domain by using the gravity wave dispersion relation

$$m^2 = \frac{(N^2 - \omega^2)}{(\omega^2 - f^2)} h^2, \tag{15}$$

where h is the magnitude of the horizontal wavenumber vector. The OH response cutoff $m \approx m_{OH} = \pi / \sigma_{OH}$ and the diffusive damping cutoff $\omega = m^2 D_{zz}$ have been transformed to the (h, ω) plane using (15) and are plotted in Figures 1b and 2b.

$$\omega = f\left[\frac{1 + (Nh/fm_{OH})^2}{1 + (h/m_{OH})^2}\right]^{1/2} \approx Nh/m_{OH} \tag{16}$$

$$\omega = [D_{zz}(N^2 - \omega^2)h^2 - \omega f^2]^{1/3} \approx D_{zz}^{1/3} N^{2/3} h^{2/3} \tag{17}$$

The approximations on the right-hand sides of (16) and (17) are valid for $f << \omega << N$. In this case, the dispersion relation simplifies to $m \approx Nh/\omega$. If we use this simplified

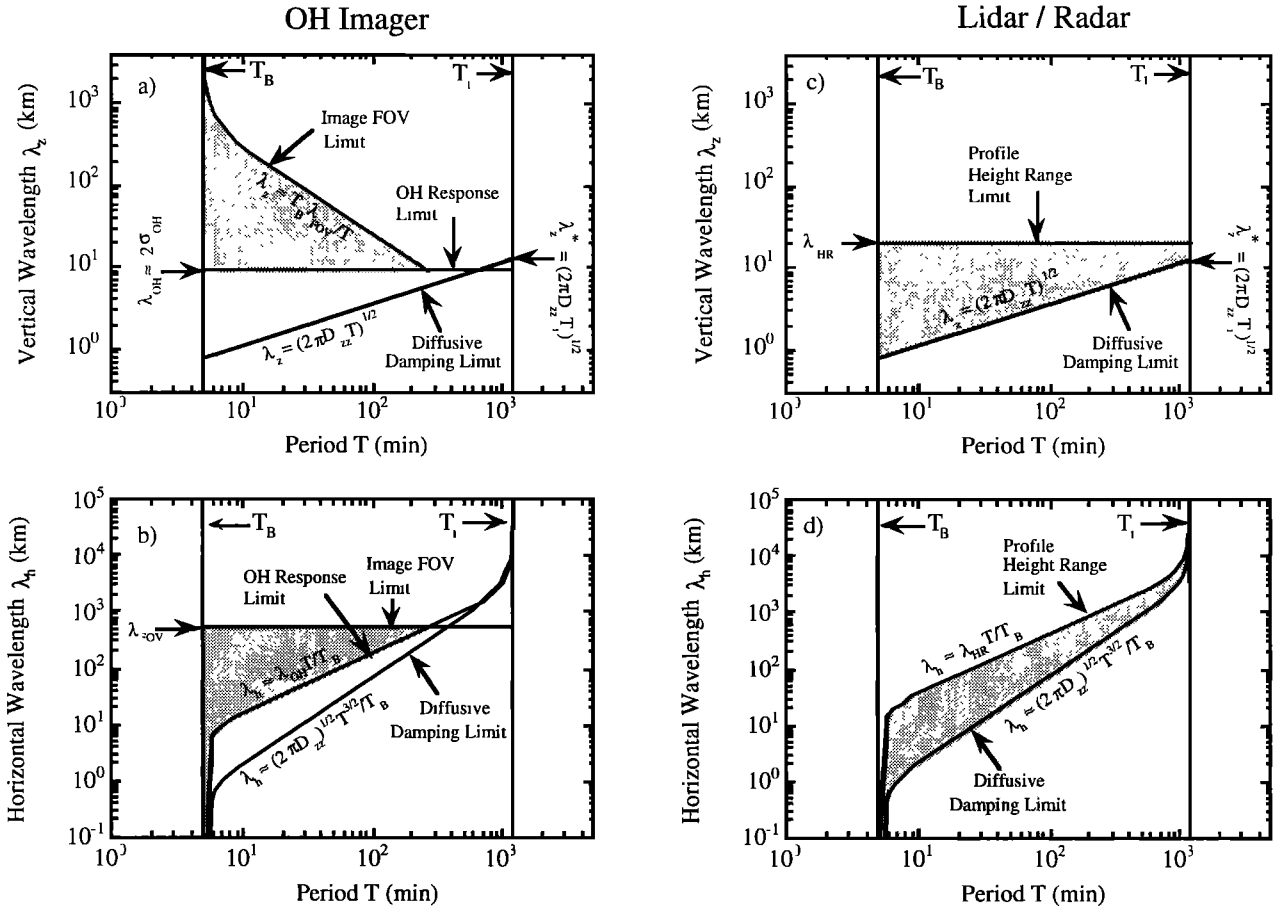

Figure 2. (a) The (λ_z, T) and (b) (λ_h, T) spectrum observation limits for OH imagers. (c) The (λ_z, T) and (d) (λ_h, T) spectrum observation limits for lidars and radars using sequences of height profiles to infer gravity wave parameters. These instruments are sensitive to gravity waves lying in the shaded spectral regions. The observation limits are plotted for $\sigma_{OH} = 4.4$ km, $\lambda_{FOV} = 500$ km, $\lambda_{HR} = 20$ km, $\lambda_z^* = 12$ km, and $D_{zz} = 320$ m^2/s.

expression in (14) and, as *Gardner* [1994] argued, assume Δm is constant, we obtain

$$\frac{<\Delta I(h,\omega)^2>}{<I>^2} \propto \exp\left[-(N\sigma_{OH}h/\omega)^2\right]\left(\frac{h}{h_*}\right)^{s-1}\left(\frac{f}{\omega}\right)^{p+3(s-1)/2},$$

$$h \le h_*\left[\frac{\omega(\omega^2/f^2-1)}{f(1-\omega^2/N^2)}\right]^{1/2} \approx h_*(\omega/f)^{3/2} \quad (18)$$

where

$$h_* = fm_*/N. \quad (19)$$

Imagers are capable of observing any waves lying to the left of both the diffusive damping and OH response limits in Figure 1b. The OH cutoff criterion given by (16) dominates and can also be expressed approximately as

$$h \le m_{OH}\omega/N \quad (20)$$

or

$$c_h = \omega/h \ge N/m_{OH}. \quad (21)$$

Imagers are most sensitive to fast horizontal phase speed waves satisfying (21). However, there is also an upper limit on the observable horizontal wavelengths associated with the imager FOV. Only waves with horizontal wavelengths smaller than the FOV can be reliably identified and characterized. The FOV limits are also plotted in Figures 1a, 1b, 2a, and 2b for λ_{FOV} = 500 km. The shaded areas represent the regions of the (m, ω) and (h, ω) spectra where imagers are most sensitive to wave perturbations. These regions are given approximately by

$$h_{FOV} = 2\pi/\lambda_{FOV} \le h \le m_{OH}\omega/N \quad (22)$$

and

$$Nh_{FOV}/\omega \le m \le m_{OH}. \quad (23)$$

Imagers observe the long vertical wavelength short-period gravity waves. Notice that the OH response and imager FOV limits intersect at $\omega \approx Nh_{FOV}/m_{OH}$ so that the longest wave period is approximately $\lambda_{FOV}T_B/2\sigma_{OH}$ or about 4.7 hours. While imagers are sensitive to longer-period perturbations, only those waves with periods shorter than $\lambda_{FOV}T_B/2\sigma_{OH}$ have horizontal wavelengths that are smaller than the FOV.

The characteristics of monochromatic gravity waves are typically determined by first looking for the distinctive wave packets in the individual all-sky images. When a wave packet is identified, its horizontal wavelength and amplitude are inferred directly from the image or from the Fourier analysis of the image [*Swenson et al.*, 1995; *Taylor et al.*, 1991a, 1995a]. Then the direction and magnitude of the horizontal phase velocity are determined by examining successive images of the wave packet. The observed period is computed from the measured horizontal wavelength and phase speed. While the imager is sensitive to all waves in the shaded area of the (h, ω) plane illustrated in Figure 1b, only those waves with amplitudes that exceed the noise limits of the instrument will be observed. In fact, the observations are biased toward the most prominent waves with the largest amplitudes. From (18) we see that for $N\sigma_{OH}h/\omega << 1$ the largest amplitude waves are the high h, low ω waves, that is, those lying close to the OH response limit.

The mean square intensity amplitude given by (18) can also be expressed as function of h and the horizontal phase speed $c_h = \omega/h$.

$$\frac{<\Delta I(h,c_h)^2>}{<I>^2} \propto \exp\left[-(N\sigma_{OH}/c_h)^2\right]\left(\frac{h_*}{h}\right)^{p+(s-1)/2}\left(\frac{f}{h_*c_h}\right)^{p+3(s-1)/2} \quad (24)$$

For a fixed h there is a distinct maximum in the mean square amplitude at

$$c_h = \frac{N\sigma_{OH}}{[p/2+3(s-1)/4]^{1/2}} \approx 70\ m/s. \quad (25)$$

The most prominent wave packets have horizontal phase speeds which lie near the OH response limit $c_h = \omega/h \approx N/m_{OH} \approx 30$ m/s in Figure 1b, where the amplitudes are largest. For these prominent waves the amplitudes are proportional to $1/h^{p+(s-1)/2} \propto \lambda_h^{p+(s-1)/2} \approx \lambda_h^{2.4}$.

Similar results are obtained if we employ the LIT spectrum model. Recall that the imager is sensitive primarily to waves in the source region of the spectrum ($m \le m_{OH} \le m_*$) where they have not yet reached saturation amplitudes. For these waves the bandwidth Δm is constant. The spectrum limits for the LIT model are the same as those plotted in Figures 1a, 1b, 2a, and 2b for the DFT model except that there is no diffusive damping limit. The mean square wave amplitudes are calculated by substituting (9) in (6) and writing the expression as a function of h and c_h using the simplified dispersion relation.

$$\frac{<\Delta I(h,c_h)^2>}{<I>^2} \propto \exp\left[-(N\sigma_{OH}/c_h)^2\right]\left(\frac{h_*}{h}\right)^{p-1}\left(\frac{f}{h_*c_h}\right)^{p+s-2} \quad (26)$$

Notice the similarity to the DFT expression in (24). For a given h the amplitude has a distinct maximum at

$$c_h = \frac{N\sigma_{OH}}{[(p+s)/2-1]^{1/2}} \approx 97\ m/s. \quad (27)$$

Again, the most prominent waves are those lying near the OH response limit where the horizontal phase speed is approximately constant. For the LIT model the mean square amplitudes of these prominent waves are proportional to $1/h^{p-1} \propto \lambda_h^{p-1} \approx \lambda_h$. Notice that this behavior is significantly different than that predicted by the DFT model. We also note that the values of these maximum phase speeds are influenced by the form assumed for the OH intensity cutoff. We used the $\exp(-m^2\sigma^2_{OH})$ form modeled by *Swenson and Gardner* [this issue]. If the cutoff is more gradual as suggested by *Schubert et al.* [1991], the values of the maximum phase speeds will decrease because the intensity perturbations would be influenced more by the higher m waves.

It is not surprising that the waves observed by imagers exhibit a narrow range of horizontal phase speeds. The intrinsic phase speed can also be related to the vertical wavenumber using the dispersion relations $c_h = \omega/h \approx N/m$. In the region $m < m_*$, both the DFT and LIT spectrum magnitudes increase with increasing m in proportion to m^s (see equations (9) and (11)), while the OH response decreases in proportion to $\exp(-m^2\sigma^2_{OH})$ (equation (6)). The combined effect is a sharply peaked response near m_{OH} or equivalently near $c_h \approx N/m_{OH}$.

6. Observational Limits for Lidars and Radars

Lidars and radars measure the height profiles of various atmospheric parameters such are temperature, winds, and density. These profiles or sequences of profiles may be used to determine gravity wave parameters. In principle, the instruments are sensitive to waves with vertical wavelengths and periods as short as the measurement resolution limits, which can approach a few minutes and a few hundred meters. They are sensitive to waves with vertical wavelengths as long as the height range of observations (λ_{HR}), and depending on how the perturbations are computed, they are sensitive to periods as long as the observation period or potentially even the inertial period. Unlike OH imagers, there are no additional limitations associated with the interactions of the waves and the atmospheric parameter being measured. We will assume the lidars and radars are sensitive to all waves with frequencies between f and N and vertical wavelengths between about 1 km and λ_{HR}. For this study we will restrict our attention to mesopause region Na lidars and radars where $\lambda_{HR} \approx 20$ km. There are other radar techniques employing multiple receivers, multiple transmitters, or beam scanning, which have quite different limitations [e.g., *Manson and Meek*, 1988]. These employ extended time sequences at single heights and correlation analyses to infer the wave parameters. Analysis of these more exotic techniques and instruments is beyond the scope of this paper.

The lidar/radar observational regimes are plotted in Figures 1c, 1d, 2c, and 2d. For the DFT paradigm these instruments are sensitive to all waves lying in the darkly shaded region between the height range and diffusive damping limits. The observational regimes for the LIT paradigm are identical except for the lack of a damping limit. If LIT is a valid description of wave dissipation, then in principle the lidars and radars should observe waves in both the darkly and lightly shaded regions. By comparing Figure 2c with the corresponding imager results in Figure 2a, we see that the imagers observe the long vertical wavelength, short-period waves, while the lidars and radars observe the short vertical wavelength waves. Their combined coverage extends over a large fraction of the gravity wave spectrum (Figure 1). Only the long vertical wavelength, long-period waves are excluded.

The characteristics of monochromatic gravity waves are typically inferred from the lidar/radar observations by first identifying the vertically propagating wave packets in the individual profiles. When a wave packet is identified, its vertical wavelength and amplitude are inferred directly from the profile or from the Fourier analysis of the profile [*Beatty et al.*, 1992; *Collins et al.*, 1996; *Nakamura et al.*, 1993]. Then the vertical phase velocity is determined by examining the wave packet in successive profiles. The observed period is computed from the measured wavelength and phase speed. In principle, the lidar or radar is sensitive to all waves in the shaded areas of the (m, ω) plane illustrated in Figure 1c. However, only those waves with amplitudes that exceed the noise limits of the instrument will be observed. Like the imager, the lidar/radar observations are biased toward the most prominent waves with the largest amplitudes. If LIT is valid, then the instruments will observe waves in both shaded areas. If DFT is valid, the waves will be restricted to the darkly shaded area to the left of the diffusive damping limit.

The mean square wave amplitudes are given by (5), (7), and (8). Since the density, temperature, and horizontal wind spectra all have the same form, we restrict our attention to the relative atmospheric density amplitudes. By using the DFT spectrum model in (5), we obtain

$$\frac{<\rho'(m,\omega)^2>}{<\rho>^2} \propto \left(\frac{m}{m_*}\right)^{s-1}\left(\frac{f}{\omega}\right)^{p+(s-1)/2}$$

$$m \le m_*(\omega/f)^{1/2} = (\omega/D_{zz})^{1/2} \qquad (28)$$

The mean square density amplitude of monochromatic waves is a monotonically increasing function of increasing m and a monotonically decreasing function of increasing ω. The largest-amplitude waves are those with the largest m and smallest ω, that is, those waves near the damping limit $\omega = m^2 D_{zz}$. The radar and lidar observations will be biased toward these prominent waves. It is important to recognize that this bias is a consequence of the amplitude distribution of the gravity waves and is not an instrument bias. The amplitudes of the prominent waves near the damping limit are proportional to $1/m^{2p} \propto \lambda_z^{2p} \approx \lambda_z^4$ and $1/\omega^p \propto T^p \approx T^2$ where T is the wave period.

The situation is quite different if we employ the LIT model spectrum. Since the lidars and radars are primarily

sensitive to the shorter vertical scale waves in the saturation region where *Dewan and Good* [1986] argued that $\Delta m \propto m$, the predicted mean square amplitude is

$$\frac{<\rho'(m,\omega)^2>}{<\rho>^2} \propto \frac{<(\rho')^2>}{<\rho>^2}\left(\frac{m_*}{m}\right)^2\left(\frac{f}{\omega}\right)^{p-1}$$

$$m \geq m_* \approx m_{HR} \qquad (29)$$

In this case, the largest-amplitude waves are those with the longest periods near the inertial period and the largest vertical wavelengths near $\lambda_{HR} \approx \lambda_z^*$. If the LIT model is valid, then the lidar/radar observations should be biased toward the low wavenumber, low-frequency waves near the intersection of the $m = m_{HR}$ and $\omega = f$ lines in Figure 1c. In this case, the mean square amplitudes are proportional to $1/m^2 \propto \lambda_z^2$ and $1/\omega^p \propto T^p \approx T^2$.

7. Comparisons With Observations

During the past decade, many observational studies of monochromatic gravity waves have been published. *Reid* [1986] and *Manson* [1990] summarized the characteristics of numerous quasi-monochromatic gravity waves observed in the mesopause region, using methods based on time series at single heights. Their data filled significant portions of the shaded areas shown in Figure 1. Unfortunately, many of the available data sets include measurements of the observed frequencies, rather than the intrinsic frequencies of the waves. Doppler effects of the background wind field can introduce errors in the inferred wave parameters.

An extensive comparison of wave parameters measured by the different instruments was published recently by *Collins et al.* [1996]. These workers compared the characteristics of 61 waves measured by the middle and upper atmosphere (MU) radar at Shigaraki, Japan (35°N) [*Muraoka*, 1988; *Tsuda et al.*, 1990; *Nakamura et al.*, 1993], 14 waves observed by an OH imager near Nederland, Colorado (40°N) [*Taylor et al.*, 1995c], and 139 waves observed with a Na lidar at Urbana, Illinois (40°N) [*Collins et al.*, 1996]. These data sets were chosen because they were acquired at roughly the same latitude and are relatively extensive (214 waves). The imager and lidar only measured the observed frequency, while the intrinsic frequency was derived from hodographs of the horizontal wind field measured by the MU radar. Even though Doppler effects can significantly alter the relationships plotted in Figure 1 for the lidar and imager data, this extensive data set does reflect the observational limits discussed previously.

The 214 waves are plotted in Figure 3 along with the various limits illustrated in Figure 1. We retain the symbolism used by *Collins et al.* [1996, Figure 13]. The solid circles are the OH imager data, the open circles are the MU radar data, and the plusses are the lidar data. In Figure 3a the imager data are roughly distributed to the left of the response limit near m_{OH}. Because of the high sensitivity of

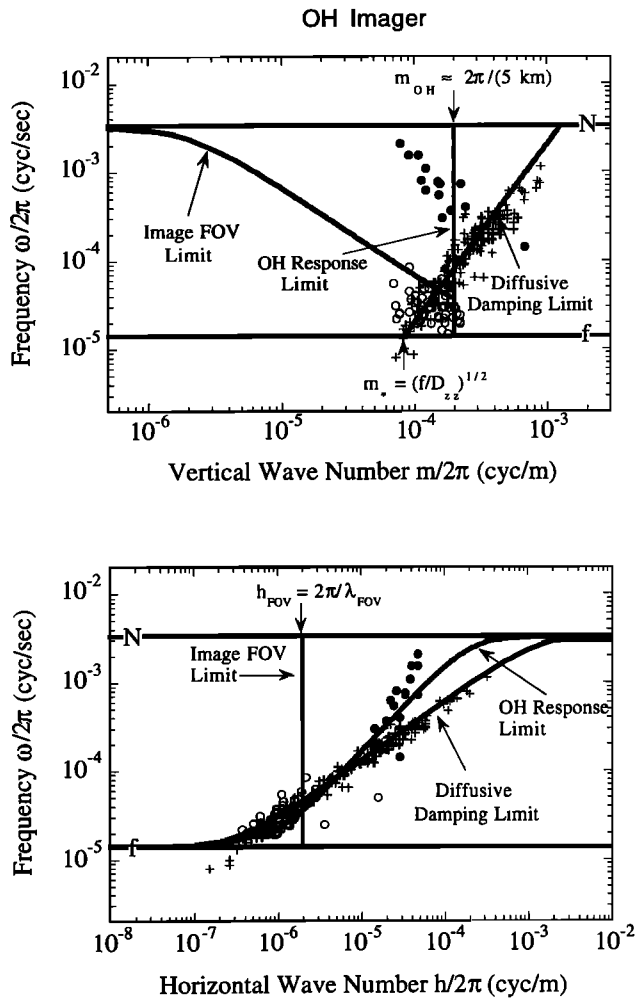

Figure 3. Monochromatic gravity waves observed at Urbana (plusses) with a Na lidar, Nederland (solid circles) with an OH imager, and Shigaraki (open circles) with the MU radar. The observation limits are plotted for m_{OH} = $2\pi/5$ km, λ_{FOV} = 500 km, λ_{HR} = 20 km, λ_z^* = 12 km, and D_{zz} = 320 m^2/s. The data are adapted from *Collins et al.* [1996].

the imager and the intense OH emissions, waves with vertical wavelengths as small as 5 km were observed. In Figure 3b the imager waves are roughly distributed along the OH response limit where their horizontal phase speeds and hence the vertical wavelengths are approximately constant. The MU radar, which observed over a height range of approximately 30 km, measured the long vertical wavelength long-period waves. The radar data in Figure 3a are clustered about the diffusive damping limit near the inertial period and λ_z^* where the wave amplitudes are maximum. In Figure 3b the radar data are distributed along the diffusive damping limit just below the height range limit but at the smaller values of h (i.e., at the larger horizontal wavelengths). The lidar data are distributed all along the diffusive damping limit in Figure 3a, from the inertial period to almost the buoyancy period. In Figure 3b the lidar waves are also distributed along the diffusive damping limit just below the height range limit. These data

are qualitatively consistent with the observational limits described in Figure 1.

Plotted in Figure 4 are histograms of the observed phase velocities for imager data acquired during the Airborne Lidar and Observations of Hawaiian Airglow (ALOHA-93) campaign at Haleakala, Maui (20°N) and during the NASA-Instituto de Pesquisas Espaciais (INPE) Guara campaign (1995) at Alacantara, Brazil (2.3°S). During both campaigns, wave data were obtained from all-sky images of the NIR OH emissions (peak altitude ~87 km), the visible OI(557.7 nm) emissions (peak altitude ~96 km), and the visible Na(589 nm) emissions (peak altitude ~90 km). Although the same wave structures were frequently imaged in all three emissions, for this study such displays are counted as one event. The distribution of observed horizontal phase speeds for the ALOHA-93 campaign (53 events), binned in 10 m/s intervals, ranges from 20 to 100 m/s with a mean of 50 m/s. The typical measurement error is less than 3 m/s. The Guara data (49 events) exhibit a similar range of phase speeds with a mean of 48 m/s. The data from both campaigns exhibit a narrow distribution about the mean. More than 80% of the ALOHA-93 phase speeds and almost 50% of the Guara phase speeds lie within ±20 m/s of the means. This very narrow range of

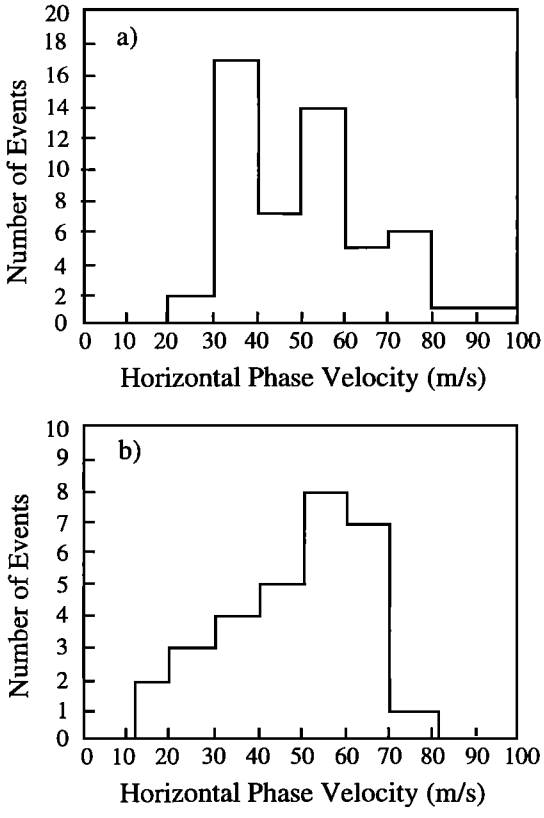

Figure 4. Histograms of the observed horizontal phase speeds for the (a) ALOHA-93 and (b) Guara campaigns. The ALOHA-93 imager data (53 events) were obtained during October 1993, while the Guara imager data (49 events) were obtained during August through October 1995.

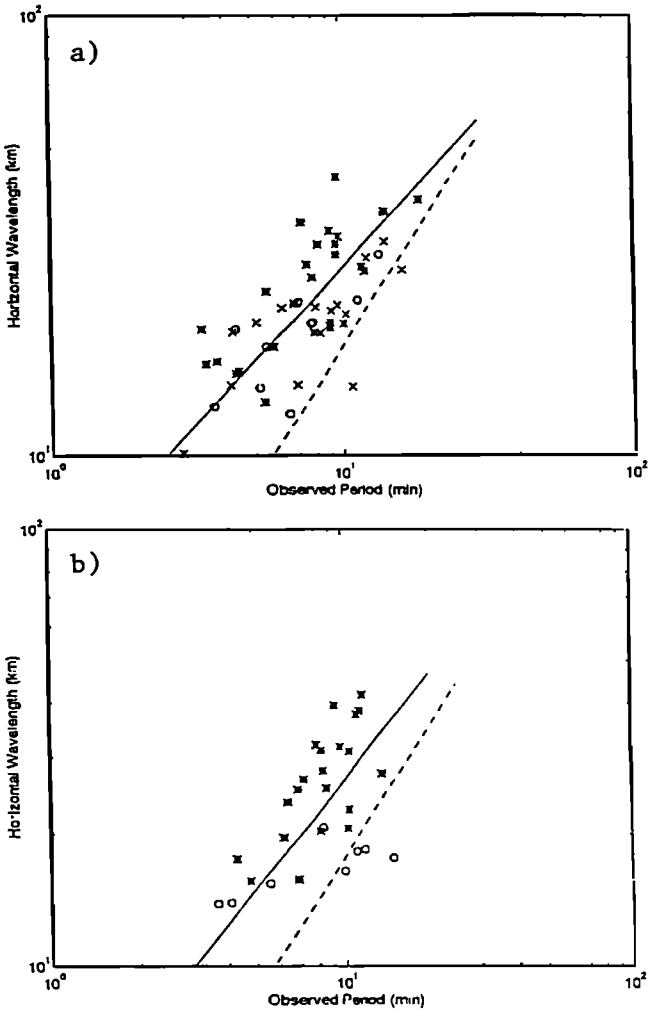

Figure 5. Distribution of intrinsic horizontal wavelength versus observed period for the (a) ALOHA-93 and (b) Guara imager data (open circles, OH image data; stars, OI image data; crosses, Na image data).

phase speeds contrasts with the wide range of possible wavelengths and periods. Gravity wave periods at these altitudes and latitudes can vary from about 5 min to tens of hours, while the horizontal wavelengths can vary from a few kilometers to several thousand kilometers. As we explained earlier, the narrow range of phase speeds is a direct consequence of the combined effects of the gravity wave vertical wavenumber spectrum and the airglow layer response characteristics.

Plotted in Figure 5 is the horizontal wavelength versus observed period for the ALOHA-93 and Guara data sets. The range and distribution of the data points are similar for both data sets. There is a clear systematic dependence of λ_h on observed period. The maximum likelihood power law fits to the data are

$$\lambda_h(\text{km}) = 5.3T_{\text{obs}}^{0.7}(\text{min}) \quad \text{ALOHA-93} \quad (30)$$

$$\lambda_h(\text{km}) = 4.0T_{\text{obs}}^{0.82}(\text{min}). \quad \text{Guara} \quad (31)$$

Also plotted in Figure 4 is the OH imager limit (dashed line) computed with $\lambda_{OH} = 2\sigma_{OH} = 8.8$ km which is

$$\lambda_h(\text{km}) = \lambda_{OH} T / T_B = 1.8T(\text{min}). \quad \text{theoretical limit} \quad (32)$$

In both cases the data lie just above the theoretical limit where the wave amplitudes are largest, in good accord with predictions. However, the imager limits were derived assuming no background wind (i.e., for intrinsic periods), while the observed data are influenced by Doppler effects of the mean wind field. Because many of the events exhibited high horizontal phase speeds (50-70 m/s) and the mean horizontal winds are typically 10-20 m/s for these altitudes (tidal winds can sometimes approach 40 m/s at these latitudes), Doppler effects should be small for these waves (except when the tidal winds, which can approach 40 m/s at these latitudes, are large) so that the observed periods should be similar to the intrinsic period. Both data sets are consistent with the observational limits illustrated in Figure 2.

8. Conclusions

Radars, lidars, and airglow imagers are all making significant contributions to our knowledge and understanding of gravity waves in the mesopause region. Each instrument is capable of observing quasi-monochromatic waves, as well as the spectra of the quasi-random perturbations in atmospheric density, temperature, and winds. We have shown that these instruments observe important but limited regions of the wave spectrum. The regions are related to the spatial and temporal limitations of the measurements and, in the case of imagers, by the response characteristics of the airglow layers. Accurate interpretation of the observations requires a clear understanding of the limits and biases of each measurement technique. Fortunately, lidars, radars, and imagers are often most sensitive to waves in largely different regions of the spectrum so that their measurements are complementary. Some of the most interesting studies are likely to emerge from wave observations in the narrow regions where the instrument sensitivities overlap and the intrinsic parameters of the waves can be completely characterized. Our analysis shows that the existing database, collected with ground-based instruments has significant limitations. Waves with periods longer than about 5 hours, vertical wavelengths exceeding 15-20 km, and horizontal wavelengths exceeding ~1000 km are not presently sampled. While powerful Rayleigh/Na lidars and mesosphere-stratosphere-troposphere (MST) radars observing over extended height ranges may be able to probe some of this spectral region, space-borne instruments such as the high-resolution Doppler imager (HRDI) and wind imaging interferometer (WINDII) on UARS are the techniques most likely to provide the key observations of these large-scale waves. Although our imager results were derived specifically for OH emissions, gravity wave imaging using the other mesospheric airglow emissions will be subject to essentially the same limitations. The only differences will be the values of the emission response limits. Since the widths of the Na, O, and O_2 airglow layers are comparable to the width of the OH layer, we expect the emission response limits for all of these emissions to be similar. The brightness of the emissions and the sensitivity of the imager also influence the response limits. Observations can be extended to shorter vertical wavelengths by employing sensitive imagers observing the brightest emissions and to longer wavelengths by employing beam swinging or multi-instrument radar techniques.

Acknowledgments. The authors thank Richard Collins and T. Nakamura for providing observational data, Jun Qian and Mark Coble for their help with the graphics, and Gary Swenson for his insights on OH layer chemistry and dynamics. The Illinois work was funded in part by NSF grant ATM 94-03036.

References

Beatty, T. J., C. A. Hostetler, and C. S. Gardner, Lidar observations of gravity waves and their spectra near the mesopause and stratopause at Arecibo, *J. Atmos. Sci., 49*, 477-497, 1992.

Coble, M., G. C. Papen, and C. S. Gardner, Computing two-dimensional unambiguous horizontal wavenumber spectra from OH airglow images, *IEEE Trans. Geosci. Remote Sens.*, in press, 1997.

Collins, R. L., X. Tao, and C. S. Gardner, Lidar observations of gravity wave activity in the upper mesosphere over Urbana, IL: Implications for gravity wave propagation in the middle atmosphere, *J. Atmos. Terr. Phys., 58*, 1905-1926, 1996.

Dewan, E. M., and R. E. Good, Saturation and the "universal" spectrum for vertical profiles of horizontal scalar winds in the atmosphere, *J. Geophys. Res., 91*, 2742-2748, 1986.

Gardner, C. S., Diffusive filtering theory of gravity wave spectra in the atmosphere, *J. Geophys. Res., 99*, 20,601-20,622, 1994.

Gardner, C. S., Scale-independent diffusive filtering theory of gravity wave spectra in the atmosphere, in *The Upper Atmosphere and Lower Thermosphere: A Review of Experiment and Theory, Geophys. Monog. Ser.*, vol. 87, edited by R. M. Johnson and T. L. Killeen, pp. 153-175, AGU, Washington, D. C., 1995.

Gardner, C. S., Testing theories of atmospheric gravity wave saturation and dissipation, *J. Atmos. Terr. Phys., 58*, 1575-1589, 1996.

Gardner, C. S., Theoretical models for gravity wave horizontal wavenumber spectra: Effects of wave field anisotropies, *J. Geophys. Res.*, this issue.

Gardner, C. S., and D. G. Voelz, Lidar studies of the nighttime sodium layer over Urbana, Illinois, 2, Gravity waves, *J. Geophys. Res., 92*, 4673-4694, 1987.

Good, R. E., Determination of atomic oxygen density from rocket borne measurement of hydroxyl airglow, *Planet. Space Sci., 24*, 389-395, 1976.

Hecht, J. H., T. J. Kane, R. L. Walterscheid, C. S. Gardner, and C. A. Tepley, Simultaneous nightglow and Na lidar observations at Arecibo during the AIDA-89 campaign, *J. Atmos. Terr. Phys., 55*, 409-423, 1993.

Hecht, J. H., R. L. Walterschied, and M. N. Ross, First measurements of the two-dimensional horizontal wavenumber spectrum from CCD images of the nightglow, *J. Geophys. Res., 99*, 11,449-11,460, 1994.

Hickey, M. P., Effects of eddy viscosity and thermal conduction and coriolis force in the dynamics of gravity wave driven fluctuations in the OH nightglow, *J. Geophys. Res.*, *93*, 4077-4088, 1988a.

Hickey, M. P., Wavelength dependence of eddy dissipation and coriolis force in the dynamics of gravity wave driven fluctuations in the OH nightglow, *J. Geophys. Res.*, *93*, 4089-4101, 1988b.

Lopez-Moreno, J. J., R. Rodrigo, F. Moreno, M. Lopez-Puertas, and A. Molina, Altitude distribution of vibrationally excited states of atmospheric hydroxyl at levels v = 2 to v = 7, *Planet. Space Sci.*, *35*, 1029-1038, 1987.

Makhlouf, U. B., R. H. Picard, and J. R. Winick, Photochemical-dynamical modeling of the measured response of airglow to gravity waves, 1, Basic model for OH airglow, *J. Geophys. Res.*, *100*, 11,289-11,311, 1995.

Manson, A. H., Gravity wave horizontal and vertical wave lengths; An update of measurements in the mesopause region (~ 80-100 km), *J. Atmos. Sci.*, *47*, 2765-2773, 1990.

Manson, A. H., and C. Meek, Gravity wave propagation characteristics (60-120 km) as determined by the Saskatoon MF radar (Gravnet) system: 1983-85 at 52°N, 107°W, *J. Atmos. Sci.*, *45*, 932-946, 1988.

McDade, I. C., E. J. Llewellyn, D. P. Murtagh, and R. G. H. Greer, Eton 5: Simultaneous rocket measurements of the OH Meinel $\Delta v = 2$ sequence and (8,3) band emission profiles in the nightglow, *Planet. Space Sci.*, *35*, 1137-1147, 1987.

Muraoka, Y., T. Sugiyama, K. Kawahira, T. Sato, T. Tsuda, S. Fukao, and S. Kato, Cause of a monochromatic inertia gravity wave breaking observed by MU radar, *Geophys. Res. Lett.*, *15*, 1349-1352, 1988.

Nakamura, T., T. Tsuda, M. Yamamoto, S. Fukao, and S. Kato, Characteristics of gravity waves in the mesosphere observed with the middle and upper atmosphere radar, *J. Geophys. Res.*, *98*, 8899-8910, 1993.

Reid, I. M., Gravity wave motions in the upper middle atmosphere (60-110 km), *J. Atmos. Terr. Phys.*, *48*, 1057-1072, 1986.

Schubert, G., and R. L. Walterscheid, Wave-driven fluctuations in OH nightglow from an extended source region, *J. Geophys. Res.*, *93*, 9903-9915, 1988.

Schubert, G., R. L. Walterscheid, and M. P. Hickey, Wave-driven fluctuations in OH nightglow from an extended, dissipative emission region, *J. Geophys. Res.*, *96*, 13,869-13,880, 1991.

Swenson, G. R. and C. S. Gardner, Analytical models for the responses of the mesospheric OH* and Na layers to atmospheric gravity waves, *J. Geophys. Res.*, this issue.

Swenson, G. R., M. J. Taylor, P. J. Espy, C. S. Gardner, and X. Tao, ALOHA-93 measurements of intrinsic AGW characteristics using the airborne airglow imager and ground-based Na wind/temperature lidar, *Geophys. Res. Lett.*, *22*, 2841-2844, 1995.

Tarasick, D. W., and G. G. Shepherd, Effects of gravity waves on complex airglow chemistries, 2, OH, *J. Geophys. Res.*, *97*, 3195-3208, 1992.

Taylor, M. J., P. J. Espy, D. J. Baker, R. J. Sica, P. C. Neal, and W. R. Pendleton Jr., Simultaneous intensity, temperature, and imaging measurements of short period wave structure in the OH nightglow emission, *Planet. Space Sci.*, *39*, 1171-1188, 1991a.

Taylor, M. J., D. N. Turnbull, and R. P. Lowe, Coincident imaging and spectrometric observations of zenith OH nightglow structure, *Geophys. Res. Lett.*, *18*, 1349-1352, 1991b.

Taylor, M. J., M. B. Bishop, and V. Taylor, All-sky measurements of short period waves imaged in the OI(557.7 nm), Na(589.2 nm), and near-infrared OH and $O_2(0,1)$ nightglow emissions during the ALOHA-93 campaign, *Geophys. Res. Letts.*, *22*, 2833-2836, 1995a.

Taylor, M. J., Y. Y. Gu, X. Tao, C. S. Gardner, and M. B. Bishop, An investigation of intrinsic gravity wave signatures using coordinated lidar and nightglow imaging measurements, *Geophys. Res. Lett.*, *22*, 2853-2856, 1995b.

Taylor, M. J., V. Taylor, and R. Edwards, An investigation of thunderstorms as a source of short period mesospheric gravity waves, in *The Upper Atmosphere and Lower Thermosphere: A Review of Experiment and Theory, Geophys. Monog. Ser.*, vol. 87, edited by R. M. Johnson and T. L. Killeen, pp. 177-184, AGU, Washington, D. C., 1995c.

Taylor, M. J., W. R. Pendleton Jr., S. Clark, H. Takahashi, D. Gobbi, and R. A. Goldberg, Image measurements of short period gravity waves at equatorial latitudes, *J. Geophys. Res.*, *102*, 26,283-26,299, 1997.

Tsuda, T., S. Kato, T. Yokoi, T. Inoue, M. Yamamoto, T. E. Van Zandt, S. Fukao, and T. Sato, Gravity waves in the mesosphere observed with middle and upper atmosphere radar, *Radio Sci.*, *26*, 1005-1018, 1990.

Walterscheid, R. L., G. Schubert, and J. M. Straus, A dynamical-chemical model of wave-driven fluctuations in the OH nightglow, *J. Geophys. Res.*, *92*, 1241-1254, 1987.

C. S. Gardner, Department of Electrical and Computer Engineering, University of Illinois at Urbana-Champaign, Urbana, IL 61801-2307. (e-mail: cgardner@uiuc.edu)

M. J. Taylor, Space Dynamics Laboratory, Utah State University, Logan, UT 84322.

(Received December 9, 1996; revised October 29, 1997; accepted November 19, 1997.)